Chondritic osmium isotope composition of early Earth mantle

P. Waterton, S.H. Serre, G. Pearson, S. Woodland, S.A. DuFrane, T. Morishita, K. Szilas

Supplementary Information

The Supplementary Information includes:

1. Samples

1.1. Chromitites

Six massive chromitite samples (208110, 208112, 208114, 208116, 208118, 208224) were collected for Re-Pt-Os isotope and highly siderophile element (HSE) analysis for this study. Massive chromitites were selected because these have the highest chromite modal abundances and correspondingly highest Os concentrations (Bennett *et al.*, 2002; Coggon *et al.*, 2015). This both makes these samples more robust to disturbance of the Re-Pt-Os isotopic systems, and facilitates the analysis of very large sample loads required for ^{186}Os analysis. The massive chromitites occur as pods which are most common towards the base of the intrusion (**Fig. 1**; Rollinson *et al.*, 2002), whereas stratiform chromitites generally occur further up. However, two chromitite pods (208116, 208118) were sampled from higher up the intrusion stratigraphy.

The chromitites primarily comprise chromite (average 92 vol. %) and phlogopite, with minor chlorite ± talc. These hydrous interstitial silicates are interpreted to have formed metasomatically either during or following amphibolite-facies metamorphism (Rollinson *et al.*, 2002), potentially associated with ~2.97 Ga or ~2.7 Ga metamorphic events recorded in the region (Rollinson *et al.*, 2002; Nutman *et al.*, 2015; Sawada *et al.*, 2023). The petrographical characteristics of chromitites from the Ujaragssuit intrusion have been described previously (Appel *et al.*, 2002; Rollinson *et al.*, 2002; Coggon *et al.*, 2015), and detailed descriptions of the samples analysed for Re-Pt-Os and HSEs in this study will be presented elsewhere.

Although all samples have experienced the effects of metamorphism and are altered from their primary compositions, some samples appear more altered than others in the field. These include proximity to or intrusion by large leucogranite sheets, proximity to more heavily altered ultramafic rocks from within the Ujaragssuit intrusion, and strong foliations imparted by alignment of mica (phlogopite) in the chromitites. We therefore subdivided the chromitites into a 'fresh' (*i.e.* relatively well-preserved) group and an 'altered group' on this basis.

1.1.1 Fresh chromitite samples

Sample 208110 (**Fig. S-1a**) was sampled from a large ~3 x 5 m chromitite pod (sample locations are shown in **Fig. 1**, with GPS coordinates reported in **Table S-1**). It is surrounded by and interfingered with dunite that dominates the lower part of the Ujaragssuit intrusive sequence (Rollinson *et al.*, 2002). The pod is massive and appears relatively fresh in the field. Sample 208112 (**Fig. S-1b**) was sampled from a ~3 x 7 m chromitite pod. Although it is bounded in places by dunite, it is largely surrounded by leucogranite, a sheet of which also cross-cuts the pod. The chromitite is mostly massive but locally weakly foliated. However, it appears relatively fresh away from the leucogranite contacts. Adjacent to contacts, the chromitite appears to have reacted with the intruding leucogranites to form a green amphibole-dominated rock. Sample 208118 (**Fig. S-1c**) is from a ~0.5 x 1 m chromitite pod. Contacts to the surrounding rocks are completely obscured, though nearby dunites appear relatively fresh. The chromitite is massive and also appears relatively fresh. Sample 208224 (**Fig. S-1d**) is from a ~1 x 1.5 m chromitite pod, located immediately stratigraphically below a ~5 cm thick layer of stratiform chromitite. The chromitite has a thin reaction rim along the contact with its host dunites, but otherwise appears fresh.

1.1.2 Altered chromitite samples

Sample 208114 (**Fig. S-1e**) is from a ~1 x 2 m pod. Contacts to the surrounding rocks are largely obscured, though it is at least partly bounded by intrusive leucogranite and nearby dunites appear severely altered. The chromitite has a clear foliation defined by aligned mica (phlogopite) and appears more altered, with fine veins of leucogranite intruding the chromitite in several places. Sample 208116 (**Fig. S-1f**) is from a ~2 x 5 m chromitite pod which is foliated and appears particularly mica-rich. Where contacts are exposed, it is bounded by leucogranite and occurs nearby heavily altered ultramafic rocks.

1.2. Granitoids

Six granitoid samples were selected for U-Pb analysis. These include one felsic orthogneiss sample located immediately adjacent to the Ujaragssuit intrusion (sample 208102), two more felsic orthogneisses located around 4.5 km to the west of the intrusion (208141, 208144), and three leucogranite samples that cross-cut ultramafic rocks of the Ujaragssuit intrusion. Orthogneiss samples show a clearly defined gneissic foliation with complex folding occasionally visible (**Fig. S-2a**). The orthogneisses also frequently contain pods or layers of mafic amphibolite. Leucogranites adjacent to or entirely surrounded by the ultramafic rocks of the Ujaragssuit intrusion are undeformed or show a weak foliation defined by undulating biotite layers (**Fig. S-2b**). These leucogranites also cross cut and disrupt layering in both the orthogneisses and amphibolite (**Fig. S-2c**). Grain sizes in the leucogranites are variable and they can locally appear pegmatitic.

2. Methods and Data Processing

2.1. Re-Pt-Os isotope and HSE analytical methods

2.1.1 Sample digestion

Ujaragssuit chromitite samples were analysed for Re-Pt-Os isotopes and HSE abundances in three ways. The chemical separation steps following sample digestion and (where relevant) sample splitting were identical for all three methods and are described in **Supplementary Information Section 2.1.2**. The first was conventional analysis of all six chromitite samples for $^{187}Os/^{188}Os$ isotopes and HSE abundances by isotope dilution, in which ~0.2 g aliquots of chromitite powder and an appropriate amount of spike, isotopically enriched in ^{99}Ru, ^{106}Pd, ^{185}Re, ^{190}Os, ^{191}Ir, and ^{194}Pt were added to 50 mL quartz glass vials. Inverse aqua regia composed of ~2 mL concentrated HCl (10.6 M) and ~5 mL concentrated HNO_3 (15.4 M) was added to the vials. The vials were closed with a semi-permeable Teflon seal and heated to 260 °C at a containing pressure of ~130 bar for 16 hours in a high pressure asher (HPA), to digest HSE bearing phases and equilibrate the spikes and samples. The digested chromitite then underwent chemical separation and analysis of both Os isotopes and HSE abundances.

Table S-1   Sample locations and summary. Apparent ages are weighted mean Re-Os model ages (**Section 2.2 in the main text**) for massive chromitites and interpreted igneous zircon U-Pb ages (**Supplementary Information Section 3**).

Sample	Lithology	Chromitite classification	Chromitite pod size	Latitude	Longitude	Apparent ages
208110	Chromitite	fresh	~3 x 5 m	64.937678	-49.988624	3226.6 ± 1.7 Ma
208112	Chromitite	fresh	~3 x 7 m	64.937364	-49.987883	3244.2 ± 1.2 Ma
208114	Chromitite	altered	~1 x 2 m	64.937316	-49.987596	3181 ± 8 Ma
208116	Chromitite	altered	~ 2 x 5 m	64.936872	-49.987634	3046 ± 123 Ma
208118	Chromitite	fresh	~0.5 x 1 m	64.938037	-49.991405	3230.9 ± 1.9 Ma
208224	Chromitite	fresh	~1 x 1.5 m	64.937521	-49.987931	3240.7 ± 2.1 Ma
208102	Orthogneiss			64.936856	-49.986451	~3.8 Ga
208141	Orthogneiss			64.948645	-50.081768	3849 ± 6 Ma
208144	Orthogneiss			64.949867	-50.089679	3842 ± 7 Ma
208158	Leucogranite			64.937801	-49.991258	2966 ± 6 Ma
208159	Leucogranite			64.937801	-49.991258	2976 ± 6 Ma
208234	Leucogranite			64.936730	-49.986850	2976 ± 8 Ma

The second approach was a split analysis, performed for only four of the chromitite samples. In this approach, the majority of the sample remained unspiked for high precision analysis of radiogenic and stable Os isotopes, including $^{186}Os/^{188}Os$, but a small subsample was spiked after the initial sample digestion for analysis of HSE abundances and ratios by isotope dilution, in particular Pt/Os and Re/Os. Approximately 2 g aliquots of chromitite powder were added to 90 mL quartz glass vials without an isotopic spike. The vials were sealed as described above and HPA digestion was also conducted at 260 °C and ~130 bar for 16 hours. However, 14 mL of inverse aqua regia was used, comprising ~4 mL concentrated HCl and ~10 mL concentrated HNO_3. This quantity of aqua regia was found to dissolve all visually identifiable chromite in these samples, though a fine grey silicate powder, likely comprising phlogopite that is petrographically observed in the Ujaragssuit chromitites, remained in the base of the vials. Experiments with larger quantities of sample powder (~5 g) with the same volume of acid left significant residual undissolved chromite. To prevent the loss of volatile Os from the unspiked samples, following the digestion they were immediately and rapidly cooled after removal from the asher by placing the 90 mL quartz vials in a partially frozen slurry of water and ethanol at -18 °C. Approximately 10 % of the digested chromitite sample, comprising 1.4 mL of aqua regia, was pipetted into 50 mL quartz glass vials containing an appropriate amount of isotopic spike and 2.5 mL of concentrated HNO_3. The vials were sealed before a short 1 hour digestion at 260 °C and ~130 bar to ensure equilibration of the spike and dissolved chromitite sample. This produced two sample splits: an unspiked aliquot, comprising around 90 % of the sample, that only underwent chemical separation and analysis of Os isotopes, and a spiked aliquot, comprising around 10 % of the sample, that underwent chemical separation and analysis of both Os isotopes and HSE abundances.

Figure S-1 (a–d) 'Fresh' and (e, f) 'Altered' chromitite samples analysed for Re-Pt-Os isotopes and HSE abundances in this study. **(a)** Sample 208110, **(b)** Sample 208112, **(c)** Sample 208118, **(d)** Sample 208224, **(e)** Sample 208114, **(f)** Sample 208116. Cross-cutting leucogranites are labelled as 'granite'.
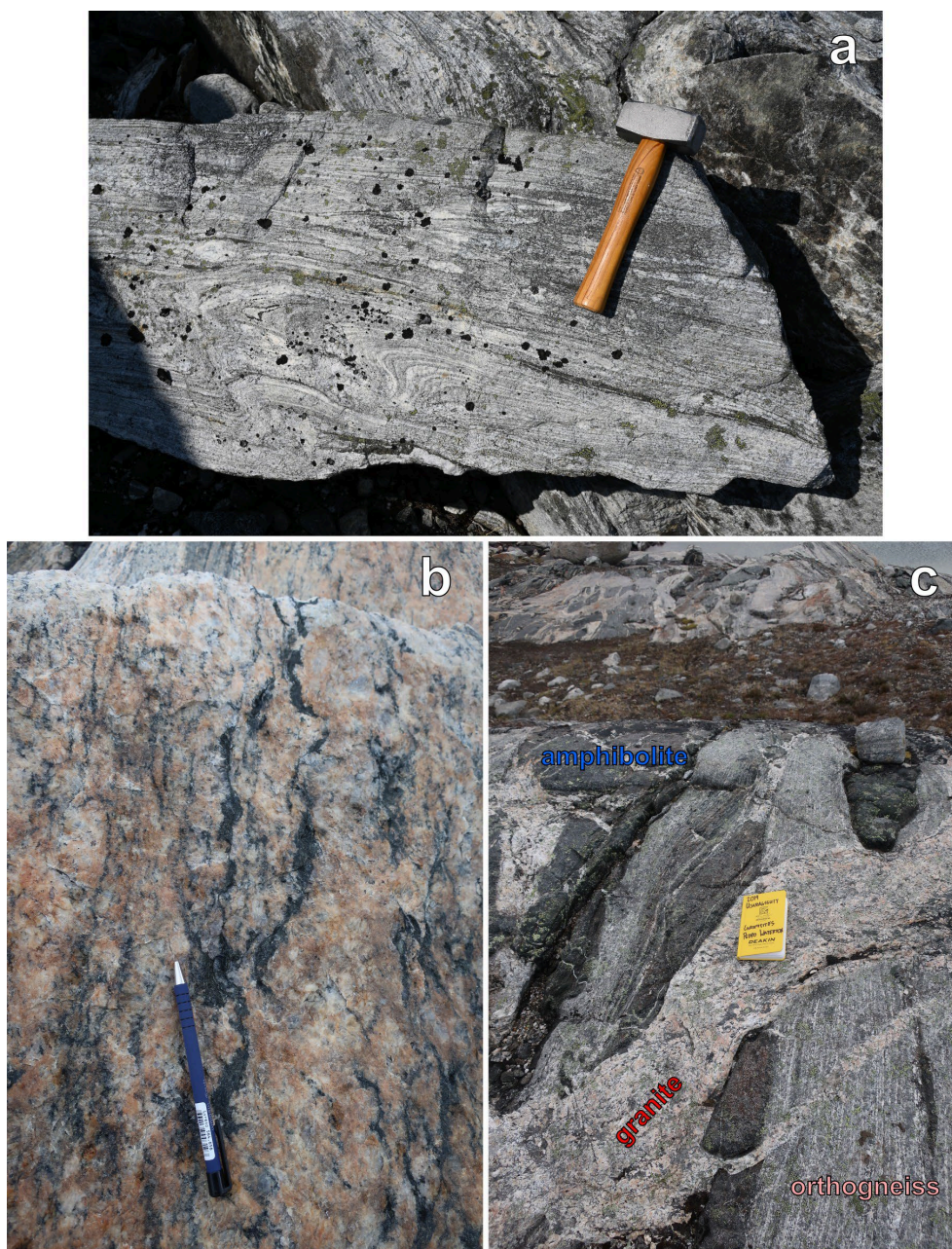
Figure S-2   **(a)** Complex folding visible in an orthogneiss boulder, adjacent to location of sample 208144. **(b)** Leucogranite with weak foliation defined by wavy biotite layers, near southern edge of Ujaragssuit intrusion. **(c)** Leucogranite cross-cuts both felsic orthogneiss and mafic amphibolite, adjacent to western edge of Ujaragssuit intrusion.

Following the recognition that consistently low Pt/Os and Re/Os in the Ujaragssuit chromitites had a negligible effect on Pt-Os and Re-Os model ages (**Supplementary Information Sections 2.2.2**, **2.2.3**), the majority of high precision Os isotope analyses (20 total replicate analyses of the six chromitite samples) were simply conducted on unspiked samples without measuring HSE abundances or ratios. These samples were initially treated in the same way as the split analyses, with 2 g aliquots of chromitite powder dissolved in 90 mL quartz glass vials without isotopic spike, digested in a HPA at 260 °C and ~130 bar for 16 hours. However, after removal from the HPA, 100 % of the digested sample was retained for chemical separation and analysis of Os isotopes.

Analyses of the same samples using the conventional isotope dilution analysis and the split spiked/unspiked analysis shows that HSE concentrations in the split analyses are consistently lower, with the exception of Pt (**Fig. S-3**). Osmium concentrations are on average 14 % lower in the split analyses, whereas Ir, Ru, and Pd are 27 %, 18 %, and 37 % lower,

respectively. Because Pt abundances are identical between the conventional and split analyses (the 1 % average difference is within analytical uncertainty), this results in higher Pt/Os in the split analyses. These differences are unlikely to result from nugget effects in the samples, as this should cause scatter either side of a 1:1 line, with some split analyses being higher than the conventional analyses. These are also unlikely to result from loss of volatile Os between the unspiked and spiked digestions, because Ir, which is not volatile, shows a similar loss. Instead, we suggest that spikes and samples are able to completely isotopically equilibrate during digestion for the conventional analyses, even if HSE bearing phases are not be completely digested. In the split analyses, where the spike and sample are not isotopically equilibrated during digestion and the spike is added later, the spiked aliquot only 'sees' the HSE concentrations that were fully liberated into the aqua regia. This loss of HSEs in the split analyses appears more significant than any potential nugget effects present in the samples. For this reason, we use HSE abundances and Pt/Os determined by conventional isotope dilution analyses for throughout this paper, including for calculation of Pt-Os model ages (**Supplementary Information Section 2.2.3**).

2.1.2   Chemical separation of Os and other HSEs

Following sample digestion, Os was separated using $CHCl_3$ solvent extraction, back extracted into HBr (Cohen and Waters, 1996), and purified by micro-distillation (Birck *et al.*, 1997). The purified Os residues were dissolved in 1 μL of concentrated HBr and loaded on high purity outgassed Pt filaments, along with 1 μL of $NaOH–Ba(OH)_2$ activator, for analysis by negative ion thermal ionisation mass spectrometry (N-TIMS).

Following Os extraction, the aqua regia was dried before converting the HSEs to chloride form by drying repeatedly in HCl. Matrix separation was achieved using anion exchange chromatography modified from Pearson and Woodland (2000). The separate HSE fractions were dissolved in either 0.8 N HNO_3 (Re-Ru and Pt-Ir cuts) or 0.5 N HCl (Pd cut) for analysis by solution inductively-coupled-plasma mass spectrometry (ICP-MS).
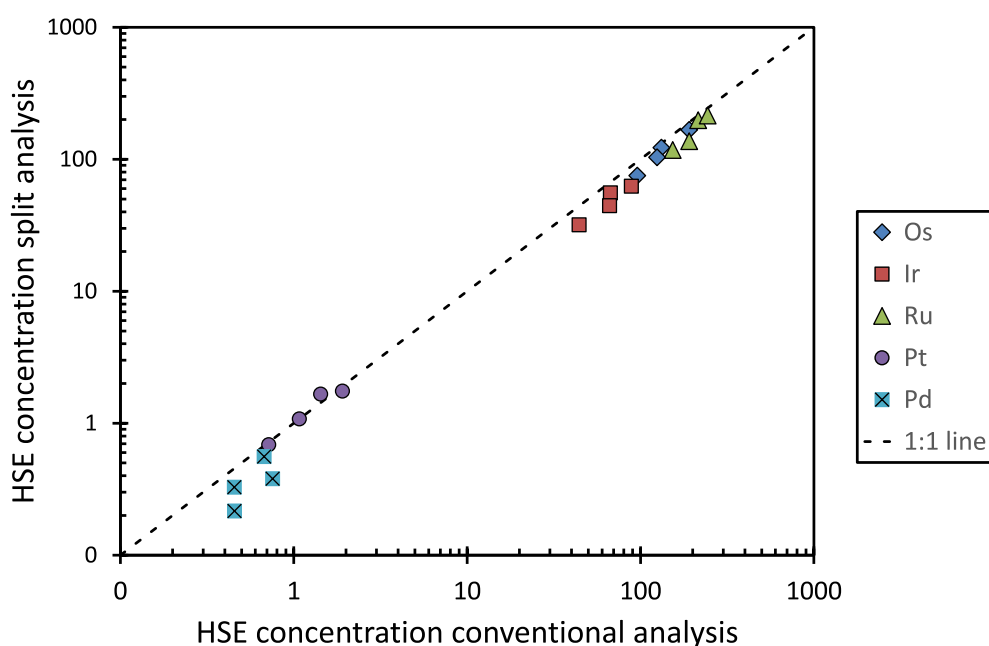
Figure S-3   Comparison of HSE abundances determined by conventional isotope dilution analysis and split spiked/unspiked analysis.

2.1.3   Analysis of HSE abundances and ratios

Highly siderophile element abundances (excluding Os) were analysed on a Nu Attom ICP-MS at the Arctic Resources Geochemistry Laboratory at the University of Alberta (ARGL). Mass fractionation was corrected externally using synthetic 1 ppb HSE standards. The mass fractionation-corrected isotopic composition of these standards show

repeatabilities of <0.3 % for Re, Pt, and Ir, <0.6 % for Ru, and <0.9 % for Pd (2 relative standard deviations). We take these values as the maximum precision on an individual isotopic measurement and propagate these uncertainties into the final HSE abundance data.

Blank corrections were made based on long term average blanks (n = 22; **Table S-2**) for all abundance and isotopic analyses, with uncertainties propagated into all HSE abundance and Re-Os isotopic data. Despite using a long term average, blanks were monitored for each analytical session to identify any potential contamination. Blanks contribute <0.03 % of the total mass analysed for Os, Ir, and Ru, and blank corrections are negligible for these elements. However, blanks contribute up to ~23 % of the total mass analysed for Pt and Pd (average of 12 % and 15 %, respectively), and are the major source of uncertainty in data for these elements. The situation is even more drastic for Re; for most samples blanks represent the majority of the total mass analysed. This resulted in all but one sample (208116) having Re below the limit of detection (LOD; defined as the analytical blank plus three standard deviations) of 6.9 pg, and two of six samples (208118 and 208224) having measured Re signals that were lower than the analytical blank of 1.8 ± 3.4 pg. The Re abundances for these samples are therefore highly imprecise or could not be calculated at all. Fortunately, the extremely low Re concentrations mean that this has a negligible effect on Re-Os model ages (**Supplementary Information Section 2.2.2**). Rhenium data collected from the four analyses split into spiked and unspiked aliquots was associated with an anomalously high analytical blank (32.7 ± 2.7 pg) and Re concentrations that were much higher than analyses using the conventional HSE abundance approach. We therefore believe these analyses were affected by Re contamination and do not use their Re data in this study.

Accuracy of the HSE abundance measurements (including Os) was monitored through repeat analyses of the OKUM standard. The intermediate precision (JCGM, 2008) is better than 17 % (2 relative standard deviations, n = 57) for all HSEs, which includes uncertainty from powder heterogeneity (**Table S-2**). Our data overlaps previously published data for the OKUM standard within 2 standard deviations (Geo Labs, 2001; Barnes and Fiorentini, 2008; Maier *et al.*, 2009; Savard *et al.*, 2010; Waterton *et al.*, 2021), and we consider the data accurate at this level of precision.

2.1.4 *Analysis of conventional Os isotopes for $^{187}Os/^{188}Os$*

Os isotopes and abundances were measured using negative thermal ionization mass spectrometry (N-TIMS; Creaser *et al.*, 1991) on a Thermo Fisher Triton Plus at the ARGL. As all samples had high Os abundances, measurements were undertaken using Faraday Cups (FC) equipped with 10^{12} Ω resistors (Liu and Pearson, 2014); analytical blanks were analysed by peak hopping on a secondary electron multiplier (SEM). Mass fractionation was corrected to $^{192}Os/^{188}Os$ = 3.083. Accuracy and precision of the Os isotope analyses was assessed through repeated measurements of the DROsS reference material, which yielded long term mean values of $^{187}Os/^{188}Os$ = 0.160938 ± 0.000072 (2s absolute; n = 34; 2s relative = 0.45‰) for FC analyses of 500 pg–2.5 ng standards, and $^{187}Os/^{188}Os$ = 0.16083 ± 0.00026 (2s absolute; n = 49; 2s relative = 1.6‰) for SEM analyses. The mean $^{187}Os/^{188}Os$ for DrOsS analysed both using FC and SEM overlap with the accepted value of 0.1609227 ± 0.0000022 (Luguet *et al.*, 2008; Waterton *et al.*, 2023) within 2 standard deviations; the Os isotopic data are accurate at this level of precision.

2.1.5 *High precision radiogenic and stable Os isotopes*

High precision analyses of radiogenic and stable Os isotopes were also conducted using N-TIMS on the same Thermo Fisher Triton Plus at the ARGL. Detailed descriptions of the analytical protocols, sources of error, potential interferences, and repeat analyses of the DROsS reference material interspersed between the sample analyses are provided in Waterton *et al.* (2023). The samples were measured in three magazines that correspond to the three magazines analysed in 2021 from Waterton *et al.* (2023), we refer to these as magazines 1–3 throughout these methods. The size of DROsS load used (50–100 ng) was chosen to be similar to the expected sample load from the 2 g samples (~200–400 ng), allowing for some loss of Os during sample digestion and purification.

Samples dissolved in 1 μL HBr were loaded onto high purity outgassed Pt filaments and dried, before addition of 1 μL of NaOH–Ba(OH)₂ activator to entirely cover the sample load. Osmium isotopes were analysed as OsO_3^- trioxides in static mode at high beam currents (>100 mV ^{186}Os), with analyses of potential Pt-Re-W interferences performed before and after each run. For the majority of samples, O isotopes were also measured before and after each run, but in some early analyses the O isotope measurement before the run failed due to a peak centring failure at high beam currents.

All samples were analysed using long baselines (Chatterjee and Lassiter, 2015), with either a ~20 minute baseline (1200 cycles of 1.05 s each) measured every 600 signal integrations (8.39 s each), or a ~30 minute baseline (1800 cycles) measured once before the run, with these runs limited to 600 cycles in total. Long baselines (~20 or 30 minutes) were also analysed before O isotope analyses. Most samples, except for three samples with insufficient Os for high precision isotope analysis, were analysed for 600–2400 signal integrations (8.39 s each), with analyses being cut off once the ^{186}Os signal fell below 100 mV, or, in the 30 minute baseline analyses, after 600 cycles. All sample analyses used 10^{11} Ω amplifiers for the isotopes from ^{186}Os to ^{192}Os, while a 10^{12} Ω amplifier was used for ^{184}Os. This allows particularly precise analyses of ^{184}Os/^{188}Os, but has the drawback on preventing amplifier rotations from being used and increasing the uncertainty associated with measuring amplifier gain factors (Waterton *et al.*, 2023). Amplifier gain factors were measured during filament heating before every analysis. Details on the exact duration of baseline and signal integrations, O isotopes, and magnitude of interference correction for each sample are reported in **Table S-3**.

2.2. Os data processing

2.2.1 *High precision radiogenic and stable Os isotopes*

Data processing followed the protocols used for analyses of the DROsS reference material described by Waterton *et al.* (2023). Raw Os isotopic data were corrected for PtO$_2$ interferences, stripped of multiple oxygen isotope interferences, renormalised and fractionation corrected, before being screened for signal intensity (*i.e.* ^{186}Os signal >100 mV) and outliers using a median absolute deviation (MAD) filter (Huber, 1981; Leys *et al.*, 2013). Data was fractionation corrected to ^{192}Os/^{188}Os = 3.083 (Brandon *et al.*, 2006; Luguet *et al.*, 2008) assuming an exponential mass fractionation law.

No blank correction was made for the high precision Os isotopes, because concentrations were not determined for these Os aliquots, and it is not possible to analyse the ^{186}Os/^{188}Os and stable isotope ratios of the blank with sufficient precision to make a meaningful correction. However, because the high precision Os analyses use ~10 times more sample than the conventional Re-Os and HSE abundance analyses or spiked portion of the split analyses, the blank contribution to the total Os in these analyses is expected to be a factor of 10 smaller. The blank contribution based on Os concentrations determined in the spiked analyses is negligible, with an average blank contribution of 0.0017 % and no sample exceeding 0.003 %.

Similar to the DROsS standard, plots of processed ^{184}Os/^{188}Os against ^{186}Os/^{188}Os are uncorrelated when no correction is applied for WO$_3$ interferences, but become weakly correlated when WO$_3$ is corrected for (**Fig. S-4**). Although the correlation is weak, this behaviour is identical to that seen in repeated analyses of the DROsS reference material, which showed a statistically significant correlation due to a greater range in signal measured on mass 231 (potentially ^{183}WO$_3$) and a greater number of analyses for DROsS. The introduction of a correlation between ^{184}Os/^{188}Os and ^{186}Os/^{188}Os when WO$_3$ interferences are corrected for suggests that this interference is not real, and the signal measured on mass 231 has another source rather than ^{183}WO$_3$. Data presented in this paper is therefore not corrected for WO$_3$ interferences. As in Waterton *et al.* (2023), we could not robustly rule out a ReO$_3$ interference on ^{187}Os. However, if signal measured on mass 233 is assumed to entirely represent ^{185}ReO$_3$, the average magnitude of the ReO$_3$ correction on ^{187}Os is 54 ppm. This increases Re-depletion ages (T_{RD} ages; **Section S-2.2.2**) by an average of 0.8 Myr, which is negligible given the systematic uncertainties associated with these ages. Given that DROsS reference material data becomes more scattered when a ReO$_3$ correction is made (Waterton *et al.*, 2023), we do not apply a ReO$_3$ correction to our data.

As observed for the DROsS reference material (Waterton *et al.*, 2023), O isotopes are time dependent, with those analysed before the high precision Os isotope runs being isotopically heavier than those measured after the run (**Fig. S-5**). Despite this, ^{17}O/^{16}O is strongly correlated with ^{18}O/^{16}O. This cannot be explained by Rayleigh fractionation of O from either the loading materials or tank, and was interpreted by Waterton *et al.* (2023) to represent mixing between oxygen sourced from the NaOH–Ba(OH)$_2$ activator and oxygen bleed tank. When plotted against the time since first analysis (used as a proxy for how long the filament had been hot), the data is more scattered than the tight correlations seen for the DROsS reference material. However, we interpret this to reflect the much more variable behaviour of samples during heating compared to the reference material; different samples likely have different Os yields during chemistry, and require variable filament temperatures to reach sufficient Os beam currents for high precision Os analyses.

To account for this time variable behaviour, O isotope compositions are time interpolated for all Os analyses with successful O isotope analyses before and after the run. For the few analyses where O isotopes were only successfully measured after the run, O isotopes are extrapolated back across the duration of the run using the average gradients in $^{17}O/^{16}O$ and $^{18}O/^{16}O$ against time, determined for the DROsS reference material (**Eqs. S-1** and **S-2**).

$$^{17}O_t = -7.7 \times 10^{-11} t + 0.0003844, \qquad \text{(S-1)}$$
$$^{18}O_t = -8.01 \times 10^{-10} t + 0.002024, \qquad \text{(S-2)}$$

These are equivalent to Equations 13 and 14 in Waterton *et al.* (2023), but determined more precisely using the average tank oxygen value (rather than the Nier, 1950 oxygen isotope composition) to strip multiple oxygen interferences from masses 240, 241, and 242 for calculation of $^{17}O/^{16}O$ and $^{18}O/^{16}O$.
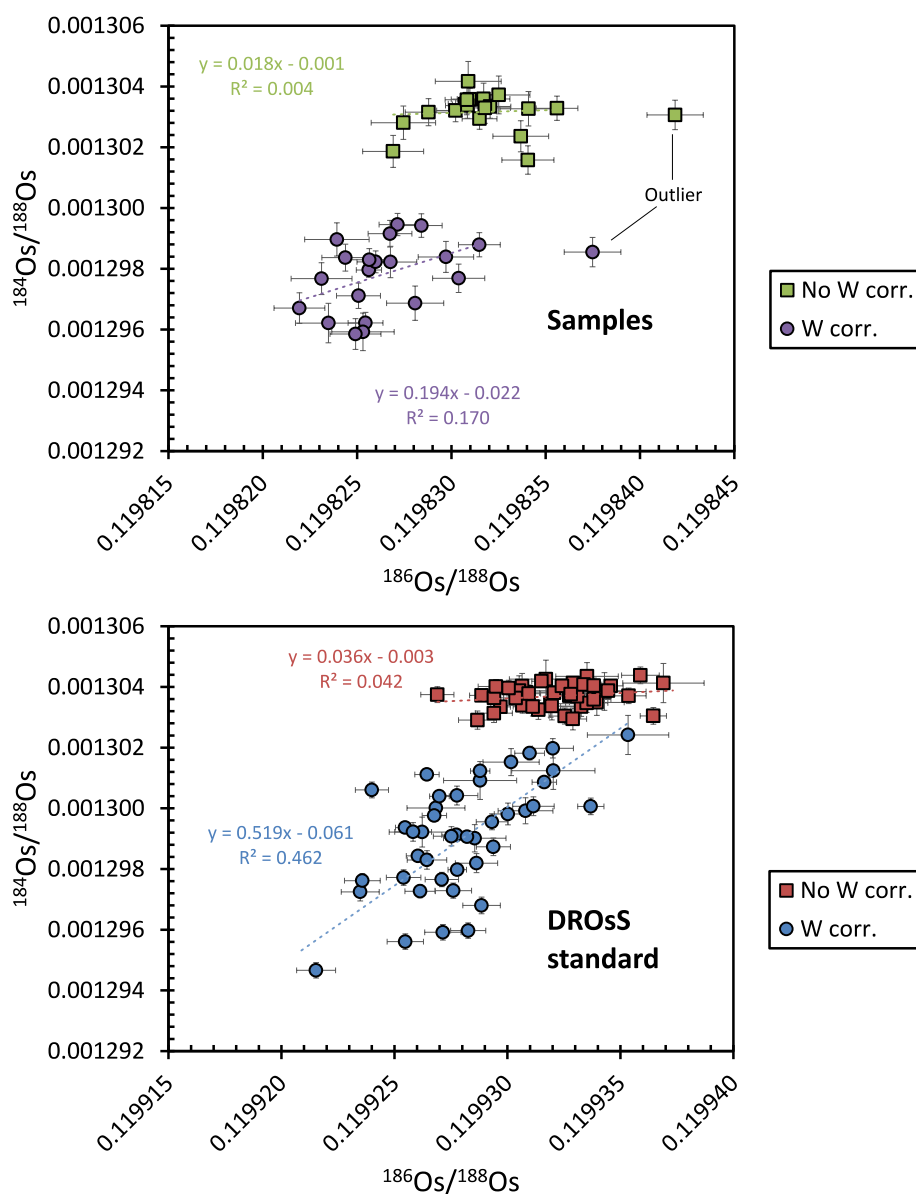
Figure S-4 Plots of $^{184}Os/^{188}Os$ against $^{186}Os/^{188}Os$ for samples from this study and DROsS reference material (Waterton *et al.*, 2023) measured during the same analytical campaign. Both show no correlation ($R^2 \sim 0$) when WO_3 interferences are not corrected for, and become weakly correlated when a correction is made. One sample was a large outlier (labelled) and was not included in either regression line.
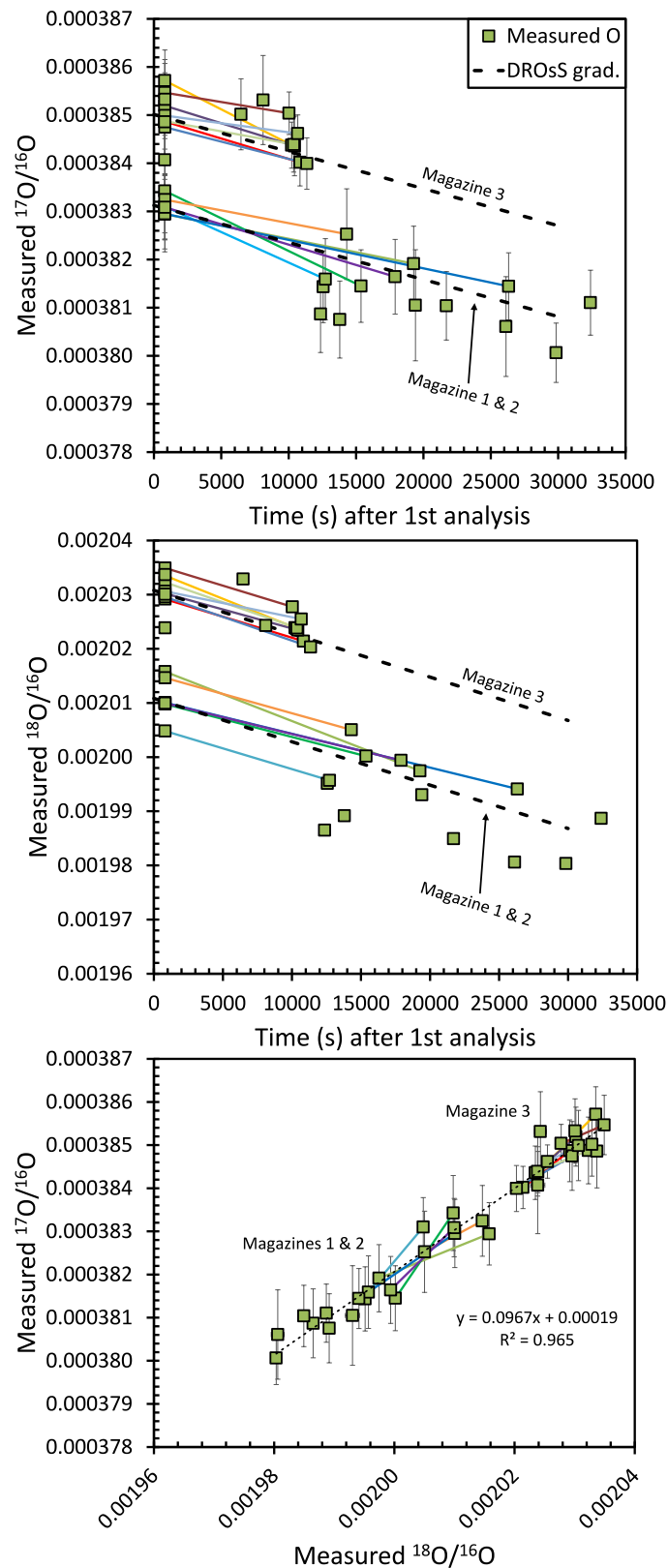
Figure S-5   Plots of O isotopes measured in conjunction with samples in this study. Coloured lines connect O isotopes measured before and after the same Os sample runs. Gradients of O isotopes measured on the DROsS reference material against time at high temperature are shown for reference (DROsS grad.). For samples with only one successful O isotope analysis, O isotopes were extrapolated from the successful analysis parallel to these gradients.

For reasons we cannot explain, the starting $^{17}O/^{16}O$ and $^{18}O/^{16}O$ are higher in samples from magazine 3 than in those from magazines 1 and 2 (**Fig. S-5**). There were no differences in how the samples were prepared and loaded, and no such difference is seen in DROsS standards analysed in the same magazine as the samples (Waterton *et al.*, 2023). The only notable difference between magazine 3 and the other two magazines was that there was a longer time between loading and sample analysis, to allow for the possibility that Faraday cup degradation was being accelerated by running many large Os samples in a short space of time (Waterton *et al.*, 2023). It is therefore possible that O isotopes in the NaOH–Ba(OH)$_2$ activator were fractionated during a longer time at high vacuum, though it is not clear why this should affect the samples and not standards loaded using the same activator. Regardless, the O isotope composition of the samples lie on the same correlation in $^{17}O/^{16}O$ against $^{18}O/^{16}O$, and retains the same trajectory in plots of $^{17}O/^{16}O$ and $^{18}O/^{16}O$ against time once the filament is heated. Furthermore, because O isotope compositions were analysed for all successful high precision Os analyses in magazine 3 both before and after the Os runs, these differences in O isotopes can be easily corrected for.

Preliminary uncertainties were calculated for each isotopic ratio in each sample using both the "internal" precision (2 standard errors on all data with ^{186}Os >100 mV that passed the MAD outlier filter) and error propagation based on counting statistics and Johnson-Nyquist noise on baseline and signal integrations (Chatterjee and Lassiter, 2015; Waterton *et al.*, 2023). The larger of these two values was then selected for each isotopic ratio in each sample. However, these preliminary uncertainties (typically 5–15 ppm uncertainty on $^{186}Os/^{188}Os$) fail to take into account other major sources of error, including baseline drift, uncertainties arising from the gain calibration, and potential Faraday Cup degradation (Waterton *et al.*, 2023). We therefore propagate these uncertainties in quadrature with the intermediate precision of repeat analyses of the DROsS reference material from the same magazine (26–37 ppm), to produce estimates of the overall uncertainty on each analysis. This produces uncertainties between 26–40 ppm on $^{186}Os/^{188}Os$, that are used for all calculations of Pt-Os model ages and comparisons to mantle evolution curves.

Stable isotope epsilon values were calculated as the parts per 10,000 deviation from the average DROsS reference material value for DROsS measured in the same magazine as each sample, using the same methods:

$$\varepsilon^{i}Os = 10,000 * \left(\frac{\left({}^{i}Os/{}_{188}Os \right)_{sample}}{\left({}^{i}Os/{}_{188}Os \right)_{DROsS}} - 1 \right),$$

$$\textbf{(S-3)}$$

where i is the isotope of interest. Note that data are normalised to ^{188}Os, unlike many meteorite analyses that normalise to ^{189}Os, a predominantly r-process isotope (Brandon *et al.*, 2005; Reisberg *et al.*, 2009; Goderis *et al.*, 2017). This is because the data was not originally collected with a view to identifying nucleosynthetic anomalies in Os stable isotopes, and renormalising the data to $^{189}Os/^{188}Os$ simply introduces more scatter due to the uncertainty in measured $^{189}Os/^{188}Os$. Although ^{186}Os is not a stable isotope, $\varepsilon^{186}Os$ values are reported calculated relative to bulk silicate Earth at 3250 Ma after normalisation to the reference material values from Brandon *et al.* (2006; **Supplementary Information Section 2.2.3**).

2.2.2 ^{187}Os model age calculation

Unless otherwise stated, Re-Os model ages used in this paper are Re-depletion ages (T_{RD}; Walker *et al.*, 1989); all samples except for one (208116) had Re concentrations below the LOD. Even this sample has extremely low Re concentrations (0.082 ± 0.017 ppb), meaning there is only a small difference between the T_{RD} age (3006 ± 10 Ma) and Re-Os model age (T_{MA}) corrected for ^{187}Os ingrowth (3035 ± 12 Ma). This difference is negligible when systematic errors associated with the choice of Re-Os mantle model are considered (below).

All T_{RD} ages are calculated using an O-chondrite model for Earth (Walker *et al.*, 2002). Uncertainties are fully propagated including uncertainties in the measured Os and Re isotopic ratios, oxide and interference corrections, background correction (for the ICP-MS data) fractionation correction, spike unmixing calculations, spike isotopic composition and concentration, and long term variability in the DrOsS and HSE synthetic standards. Propagation of

uncertainties in the O-chondrite mantle model following Sambridge and Lambert (1997) gives a minimum uncertainty of ~600 Myr for T_{RD} and T_{MA} ages of samples aged ~3.25 Ga (assuming zero uncertainty in the measured ^{187}Re/^{188}Os and ^{187}Os/^{188}Os of the samples), primarily due to uncertainties in the O-chondrite ^{187}Re/^{188}Os. However, we believe the model ages to be more robust from this, as the differences between different chondritic reservoirs (O-, E-, and C-chondrite) or primitive upper mantle models (PUM; Meisel *et al.*, 2001) is far smaller than the uncertainty in each reservoir.

We therefore address the model-dependency of the Re-Os ages by recalculating the T_{RD} ages using different models for the Re-Os evolution of the Earth's mantle (E-chondrite, C-chondrite, PUM; Meisel *et al.*, 2001; Walker *et al.*, 2002). For ~3.25 Ga rocks, use of an E-chondrite model produces T_{RD} and T_{MA} ages ~20 Myr younger than O-chondrite; use of a C-chondrite model produces T_{RD} and T_{MA} ages ~60 Myr younger than O-chondrite; and use of a PUM mantle model produces T_{RD} and T_{MA} ages ~175 Myr older than O-chondrite. Therefore, given the ~235 Myr range in age generated by different mantle models, a more appropriate minimum uncertainty for comparison of the Re-Os ages to other geochronological data, is approximately ± 120 Myr. We propagate this uncertainty into the final T_{RD} ages in quadrature, assuming that the ± 120 Myr range is approximately equivalent to 2s uncertainty. T_{RD} and T_{MA} ages calculated from the conventional Re-Os analyses are presented along with HSE abundances and ^{187}Os isotopic data in **Table S-2**; T_{RD} ages calculated from the high precision Os isotope data are reported in **Table S-3**.

2.2.3 ^{186}Os model age calculation

For calculation of ^{186}Os/^{188}Os model ages against the Pt-Os evolution of the primitive upper mantle, data were first normalised to reference material values from Brandon *et al.* (2006), to correct for inter-laboratory differences, as with previous calculations of Pt-Os model ages at Ujaragssuit (Coggon *et al.*, 2013). However, we did not have access to high concentration solutions of the UMd reference material used by Brandon *et al.* (2006), and instead used DROsS as a reference material. We therefore normalise our data twice, first to the average DROsS ^{186}Os/^{188}Os reported by Luguet *et al.* (2008) and Coggon *et al.* (2013; who used the same analytical methods), and then by the difference in ^{186}Os/^{188}Os between UMd reference material analysed by Luguet *et al.* (2008) and UMd analysed by Brandon *et al.* (2006). The calculation can therefore be represented as:

$$\left(\frac{^{186}\text{Os}}{^{188}\text{Os}}\right)_{\text{corrected}} = \left(\frac{^{186}\text{Os}}{^{188}\text{Os}}\right)_{\text{measured}} * \frac{\left(\frac{^{186}\text{Os}}{^{188}\text{Os}}\right)_{\text{DROsS,Luguet}}}{\left(\frac{^{186}\text{Os}}{^{188}\text{Os}}\right)_{\text{DROsS,measured}}} * \frac{\left(\frac{^{186}\text{Os}}{^{188}\text{Os}}\right)_{\text{UMd,Brandon}}}{\left(\frac{^{186}\text{Os}}{^{188}\text{Os}}\right)_{\text{UMd,Luguet}}}, \qquad \textbf{(S-4)}$$

where DROsS measured is the average DROsS value measured in the same magazine as the samples. We correct our data on a magazine by magazine basis due to slight changes in the analytical protocol and resulting uncertainty between magazines (Waterton *et al.*, 2023). While this may seem like a major correction, our average DROsS value is 44 ppm higher than the average of Luguet *et al.* (2008) and Coggon *et al.* (2013), while the Brandon *et al.* (2006) UMd value is 36 ppm higher than that of Luguet *et al.* (2008). The net effect of this correction is therefore simply to shift our measured ^{186}Os/^{188}Os values down by an average of 8 ppm, which is well within the ~30–40 ppm intermediate precision of our analyses. However, this correction is essential to accurately compare our data to that of Coggon *et al.* (2013), and to calculate Pt-Os model ages, as a systematic shift in ^{186}Os/^{188}Os as small as 8 ppm is equivalent to >300 Myr of primitive upper mantle evolution (Waterton *et al.*, 2023). The lower reference material values from Luguet *et al.* (2008) and Coggon *et al.* (2013) likely reflects their use of a WO$_3$ interference correction (Waterton *et al.*, 2023), which was not applied to both our data and that of Brandon *et al.* (2006).

Following normalisation, we calculate Pt-depletion ages (T_{DA}; **Table S-3**) from ^{186}Os/^{188}Os in the same way as Re-depletion ages from the ^{187}Os/^{188}Os data. Due to the very low abundance of ^{190}Pt and its long half-life, these Pt depletion ages have very large uncertainties. If only the preliminary uncertainties of 5–15 ppm are used, the uncertainty on T_{DA} range between 238 and 620 Myr (2s; average 457 Myr). However, more realistic uncertainties of 26–40 ppm, including propagated uncertainties from repeat analyses of the DROsS reference material, give much larger uncertainties of 1125–1693 Myr (2s; average 1527 Myr) on the T_{DA} from a single analysis. Because these uncertainties are random

uncertainties, they can be reduced by averaging the ^{186}Os/^{188}Os from many replicate analyses, providing they have indistinguishable ^{186}Os/^{188}Os, before calculating the T_{DA} for the average. Excluding the two altered chromitite samples with disturbed ^{187}Os systematics (208114, 208116), T_{DA} calculated from an Isoplot weighted average of our samples' ^{186}Os/^{188}Os is 3381 ± 360 Ma (2 standard errors on the mean; n = 17; MSWD = 0.66; p = 0.84; Ludwig, 2012). Systematic uncertainties due to the ~12 ppm uncertainty in the solar system initial ^{186}Os/^{188}Os (Brandon *et al.*, 2006) are propagated into this average using error propagation after Sambridge and Lambert (1997) to yield a Pt-depletion age of 3381 ± 626 Ma, for comparison to ages from other isotopic systems.

Pt/Os in the samples ranges from 0.0075 to 0.047, corresponding to ^{190}Pt/^{188}Os between 7.1 * 10^{-6} and 4.4 * 10^{-5}. However, all but one sample (208116) have Pt/Os ≤ 0.012, or ^{190}Pt/^{188}Os ≤ 1.2 * 10^{-5}. For the vast majority of samples, the effect of ^{186}Os ingrowth since the formation of the chromitites is negligible compared to the analytical uncertainty in ^{186}Os, with the Pt mantle model ages (T_{MA}) being on average 16 Myr older than the T_{DA}. The largest difference is in sample 208116, which has T_{MA} that differ from T_{DA} by up to 44 Myr due to its higher Pt/Os. However, this sample was excluded from the average due to its disturbed Re-Os systematics. The average T_{MA}, including systematic error calculated in the same way as the T_{DA}, is 3398 ± 626 Ma.

2.2.4   Re-processing of Coggon et al. (2013)

As identified above, Pt-Os model ages are subject to massive uncertainties, even in the most optimistic case where only internal run precisions are used. Coggon *et al.* (2013) identified differences in Pt-Os model ages for three samples from Ujaragssuit, where replicates from each sample were averaged to produce Pt-depletion ages of ~4.0 Ga, ~3.5 Ga, and ~2.9 Ga. The data were further interpreted to represent two populations, an older mantle depletion event at ~4.1 Ga, and a younger regional metamorphic event at ~2.9 Ga. However, the internal run precisions reported for these analyses varied between ~17 and ~55 ppm, corresponding to uncertainties in Pt-depletion ages between 711 and 2343 Myr on individual analyses. These large uncertainties, without even considering the precision indicated by repeated measurements of reference materials, caused us to re-examine the data of Coggon *et al.* (2013), with a view to answering two questions. Firstly, can multiple events be detected beyond expected analytical scatter in the Pt-Os data? Secondly, do any of the Pt-Os data indicate Hadean mantle depletion events?

Because Coggon *et al.* (2013) also did not measure the UMd reference material, we first double normalise their data to DROsS analysed by Luguet *et al.* (2008) and Brandon *et al.* (2006), using the same procedure as for our samples to eliminate inter-laboratory biases and allow for calculation of T_{DA} relative to primitive upper mantle.

If only internal run precisions are used to estimate the uncertainty, then the Coggon *et al.* (2013) ^{186}Os/^{188}Os do not appear to represent a single T_{DA} age population at the 95 % confidence level, with an Isoplot weighted average of 3564 ± 354 Ma (2 standard errors; n = 15) giving a high MSWD of 1.88 and low probability of fit of 0.023. However, repeated analyses of the DROsS reference material by Coggon *et al.* (2013) yielding an average ^{186}Os/^{188}Os of 0.1199267 ± 0.0000043 using their double normalisation approach, indicating an intermediate precision of 35 ppm. This likely represents the best possible precision on an individual isotopic analysis, so internal precisions as low as 17 ppm for individual sample analyses are not realistic. We therefore propagate the repeatability estimated from the Coggon *et al.* (2013) DROsS data into their sample uncertainties in quadrature, using the same calculations as for our data. This results in estimated uncertainties of 40–66 ppm in ^{186}Os/^{188}Os for individual analyses. Using these new, more realistic uncertainties, the weighted average T_{DA} becomes 3558 ± 482 Ma, with a lower MSWD of 0.50 and a probability of fit of 0.94. This is consistent with the data representing a single age population at the 95 % confidence level, and we suggest there is no evidence for distinct mantle depletion and metamorphic events in the Coggon *et al.* (2013) ^{186}Os/^{188}Os data.

When systematic uncertainties due to the ~12 ppm uncertainty in the solar system initial ^{186}Os/^{188}Os (Brandon *et al.*, 2006) are propagated into the weighted average in the same manner as for our data (Sambridge and Lambert, 1997), the final T_{DA} is 3558 ± 701 Ma. While this potentially overlaps Hadean ages >4 Ga within uncertainty, this is also consistent with formation of the Ujaragssuit intrusion at much younger ages. This is discussed further in the main text.

Finally, the weighted average ^{186}Os/^{188}Os and T_{DA} from both our data and that of Coggon *et al.* (2013) closely overlap. We therefore suggest that the best estimate of the ^{186}Os/^{188}Os and T_{DA} for the Ujaragssuit intrusion is a weighted average of both our data and that of Coggon *et al.* (2013). Using our 17 samples which do not show signs of ^{187}Os

disturbance, and all data reported by Coggon *et al.* (2013), yields a weighted average $^{186}Os/^{188}Os$ of 0.1198301 ± 0.0000008 (2 standard errors on the mean; n = 32; MSWD = 0.58; p = 0.97; normalised to UMd of Brandon *et al.*, 2006). This corresponds to a T_{DA} of 3437 ± 288 Ma, or 3437 ± 587 Ma including the systematic uncertainty (Sambridge and Lambert, 1997) on the solar system initial $^{186}Os/^{188}Os$.

2.3. U-Pb analytical methods

We disaggregated ~1-2 kg of rock using a Selfrag electro-pulse open vessel disaggregation system with a 2 mm sieve. A subsample of the disaggregate was passed across a Wilfley table to concentrate dense minerals, similar to the method described by Söderlund and Johansson (2002). Between each sample great care was taken to clean the Wilfley table to reduce the risk of contamination. From the dense mineral concentrate, we hand-picked ~50 zircons to mount in epoxy. The grain mount was polished to expose the grain centres and regions suitable for analysis were identified from Cathodoluminescence imaging.

U-Pb zircon data was collected using laser ablation multi collector inductively coupled mass spectrometry (LA-MC-ICP-MS) at the Canadian Centre for Isotopic Microanalysis at the University of Alberta, Edmonton, Canada using procedures modified from Simonetti *et al.* (2005). The analytical setup consists of a New Wave UP-213 laser ablation system interfaced with a Nu plasma MC-ICP-MS equipped with three ion counters and 12 Faraday cups. We operated the laser at 4 Hz with a beam diameter of 25 μm, which yielded a fluence of ~2 J/cm^2. Ablations were conducted in a He atmosphere at a flow rate of 1 L/min through the ablation cell. Output from the cell was joined to the output from a standard Nu plasma desolvating nebulizer (DSN-100). On peak gas + acid blanks (30 s) were measured prior to a set of 10 analyses. Data was collected statically consisting of 30 integrations of 1 s each. Before and after each set of analyses, zircon reference materials LH9415 (Ashton *et al.*, 1999) and OG1 (Stern *et al.*, 2009) were repeatedly analysed, to monitor and correct for U-Pb fractionation, reproducibility, instrument drift, and to assess data quality. Mass bias for Pb isotopes was corrected by measuring $^{205}Tl/^{203}Tl$ from an aspirated Tl solution (NIST SRM 997) via the DSN-100 desolvating nebulizer using an exponential mass fractionation law and assuming a natural $^{205}Tl/^{203}Tl$ of 2.3871. All data were reduced offline using an in-house Excel-based data reduction program. Unknowns were normalized to LH9415 as the primary reference and OG1 was treated as an unknown to assess data quality (**Fig. S-6**). The uncertainties reported are a quadratic combination of the internal measurement precision and the overall reproducibility of the standards during an analytical session. The long term reproducibility for LH9415 is estimated at <1 % for $^{207}Pb/^{206}Pb$ and 2 % for $^{206}Pb/^{238}U$ (coverage factor k = 2). The data are not corrected for common Pb due to the difficulty in resolving transient contributions of ^{204}Hg present in the Ar gas from ^{204}Pb present in either the crystal and/or the acid + gas blank. Thus, reported ^{204}Pb values are for informational purposes only, but can be useful for identifying and rejecting samples that have significant contributions from Pb.
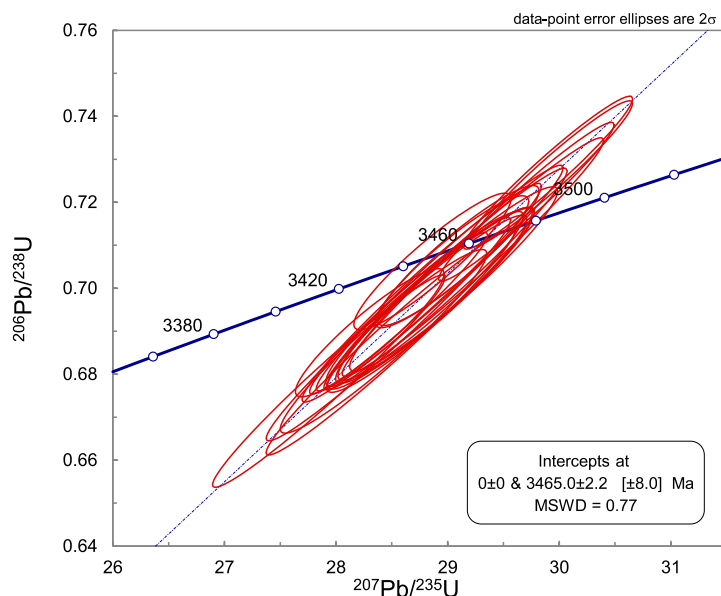
Figure S-6   Concordia diagram for OG1 data, used to assess data quality in this study. The weighted mean (Ludwig, 2012) $^{207}Pb/^{206}Pb$ age of 3465.7 ± 2.2 Ma (n = 22; MSWD = 0.78; p = 0.75) is in excellent agreement with the TIMS reference value of 3465.4 ± 0.6 Ma (Stern *et al.*, 2009). The long term excess scatter beyond weighted mean errors of the session- to-session $^{207}Pb/^{206}Pb$ weighted means is ~0.35 % (2s) for OG1.

3. Zircon U-Pb age interpretation

Zircon U-Pb spot analyses were initially screened to exclude samples with high ^{204}Pb, or anomalously high standard deviations, which could indicate ablation of inclusions or mixed analyses of domains with different ages. Data was further screened by excluding analyses with anomalously high common to radiogenic lead ratios. Thresholds of $^{206}Pb/^{204}Pb$ < 2000–3000 were used to screen the data; the exact threshold was varied between samples because some leucogranite samples have zircon with consistently low levels of radiogenic lead. Finally, the ablation time series of the remaining analyses were examined to remove mixed analyses or analyses that ablated inclusions that could not be detected in averaged data.

After screening, zircon U-Pb analyses from this study show two main clusters (**Fig. S-7**). The older lies at ~3.8 Ga and is only present in the orthogneiss samples. The younger cluster has $^{207}Pb/^{206}Pb$ ages of ~3.0 Ga and is present in both orthogneisses and leucogranites. A third, minor cluster lies at ~2.7 Ga and is only observed in leucogranite sample 208234, though we note that a number of analyses from other samples that did not pass the screening also show $^{207}Pb/^{206}Pb$ ages ranging down to ~2.7 Ga. In addition to these clusters, there is an array of $^{207}Pb/^{206}Pb$ data displaced along the concordia curve between ~3.8 and ~3.55 Ga in sample 208102, and arrays that potentially represent discordia lines between ~3.8 and ~3.0 Ga in all three orthogneiss samples, most clearly displayed in sample 208144.

Ages are assigned using the weighted mean $^{207}Pb/^{206}Pb$ age for groups that have 'acceptable' MSWD given the number of analyses in each group (Wendt and Carl, 1991; Spencer *et al.*, 2016). These are equivalent to the upper concordia intercept (with lower intercept anchored at 0 ± 100 Ma) shown in **Figures S-8 and S-9**. Groups with MSWD higher than the acceptable value are not considered to form a single age population, for example due to inclusion of zircons formed in different events, or due to variable Pb loss. The intermediate precision of the weighted mean $^{207}Pb/^{206}Pb$ of OG1 is propagated into the weighted mean $^{207}Pb/^{206}Pb$ of the samples to assign uncertainties in the final $^{207}Pb/^{206}Pb$ ages discussed in the text.
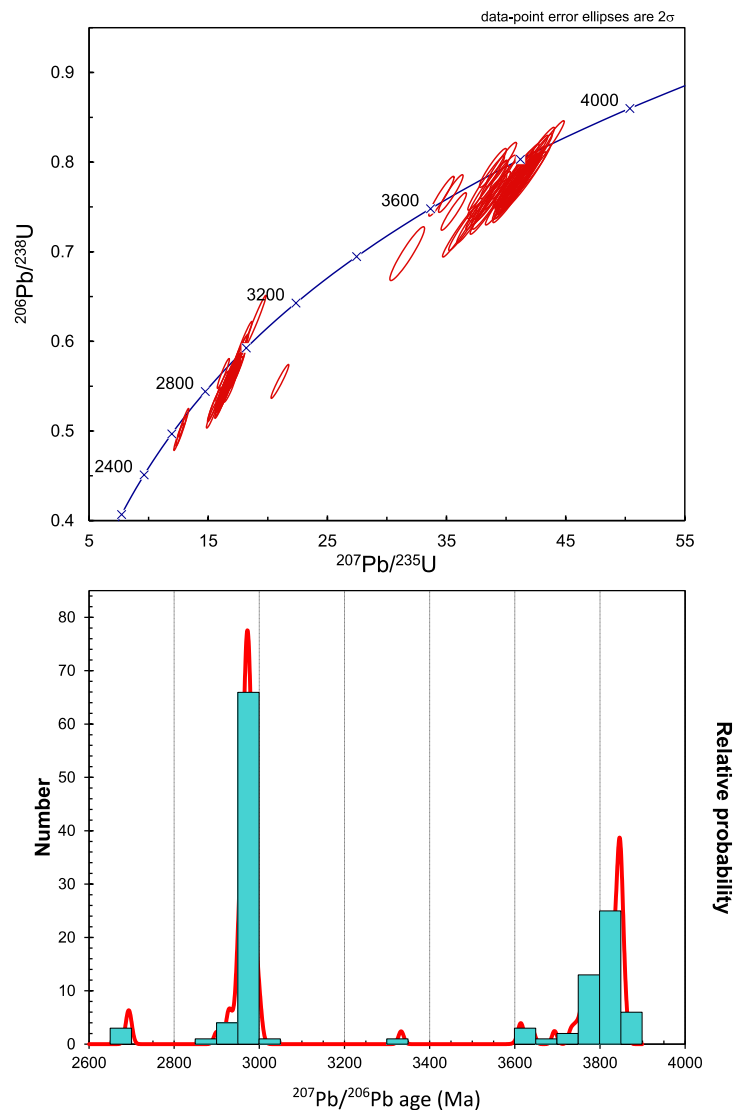
Figure S-7   Wetherill concordia diagram, and $^{207}Pb/^{206}Pb$ age probability density function and histogram (50 Myr bins) for all zircon U-Pb analyses after data screening.

3.1 Orthogneiss sample 208102

Sample 208102 does not have a clearly defined oldest age population, instead showing a broad spread of concordant ages between ~3.8 and ~3.55 Ga (**Fig. S-8a**). The oldest individual analysis has a $^{207}Pb/^{206}Pb$ age of 3794 ± 8 Ma. Given this age, the presence of clearly defined $^{207}Pb/^{206}Pb$ age groups >3.8 Ga in the other two analysed orthogneiss samples, and a previously reported igneous age of 3811 ± 5 Ma for tonalites adjacent to the Ujaragssuit intrusion (Nutman *et al.*, 1993, 1996), we tentatively infer an igneous age of ~3.8 Ga for the orthogneiss protolith. Analyses with ~3.0 Ga ages (**Fig. S-8b**) do not form a single age population in sample 208102 (weighted mean of all eight analyses has MSWD = 4.1; p = 0.0001). Instead, there are two groups with $^{207}Pb/^{206}Pb$ ages of ~2.97 and ~3.00 Ga, respectively. Weighted mean $^{207}Pb/^{206}Pb$ ages for these groups yield ages of 2972 ± 7 Ma (n = 4; MSWD = 0.16; p = 0.92) and 2997 ± 7 Ma (n = 4; MSWD = 0.21; p = 0.89), which we interpret to reflect growth of metamorphic zircon.
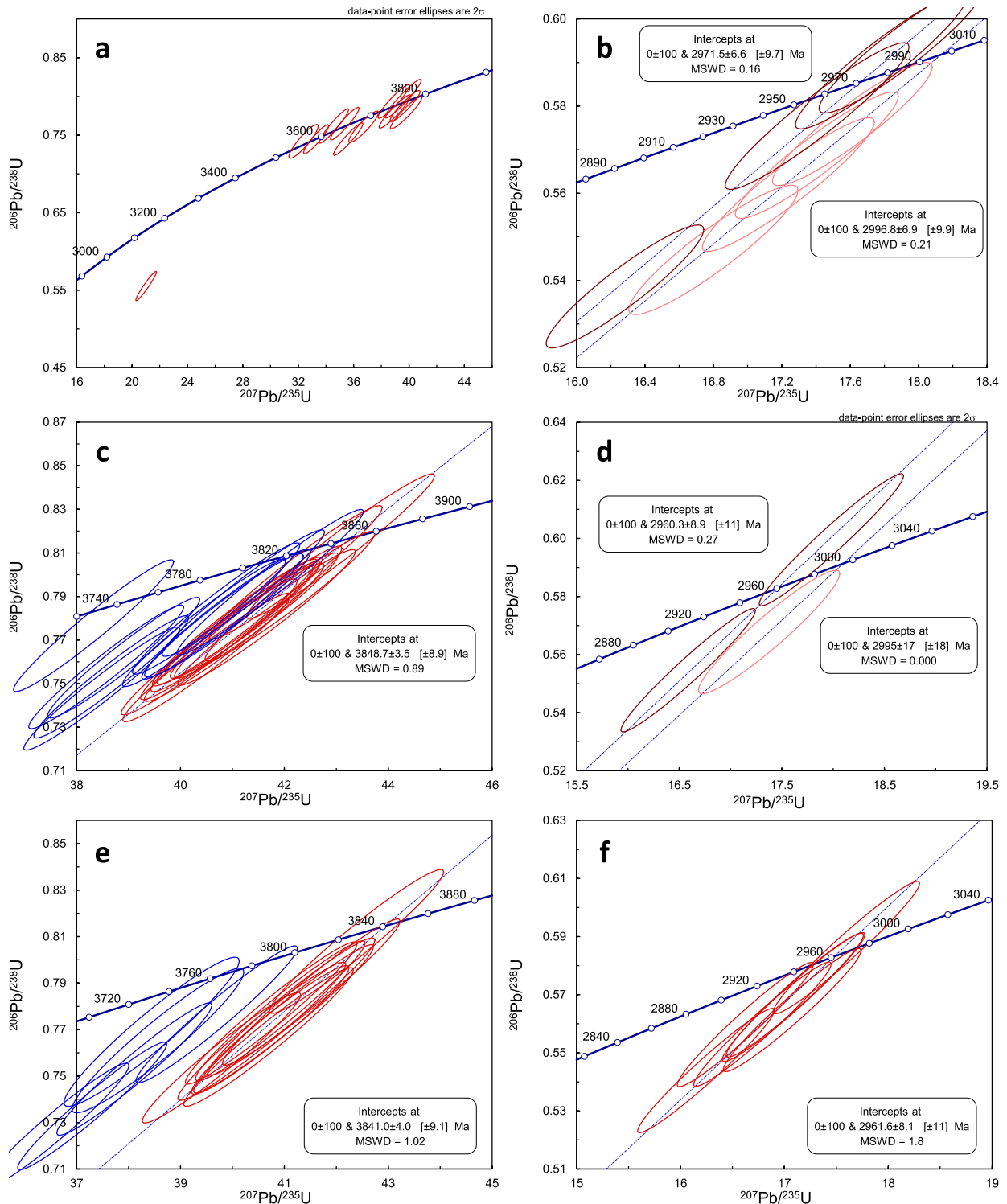
Figure S-8 Wetherill concordia plots for zircon U-Pb analyses from orthogneiss samples. Upper intercept age uncertainties shown are 95 % confidence limits calculated from the scatter in the analyses, values in square brackets include decay constant uncertainty. Blue ellipses indicate data that was excluded from regressions and weighted mean ^{207}Pb/^{206}Pb ages discussed in the text. Where two age groups are regressions are made in the same plot, light and dark red ellipses indicate older and younger groups used in the two different regressions, respectively. **(a)** >3.0 Ga analyses from sample 208102. **(b)** ~3.0 Ga analyses from sample 208102. **(c)** ~3.8 Ga analyses from sample 208141. **(d)** ~3.0 Ga analyses from sample 208141. **(e)** ~3.8 Ga analyses from sample 208144. **(f)** ~3.0 Ga analyses from sample 208144.

3.2 Orthogneiss sample 208141

The oldest age population in sample 208141 gives a weighted mean ^{207}Pb/^{206}Pb age of 3849 ± 6 Ma (n = 13; MSWD = 0.90; p = 0.54), which we interpret as the igneous age of the orthogneiss (**Fig. S-8c**). Individual analyses with ^{207}Pb/^{206}Pb ages between this igneous age and ~3.75 Ga appear to be largely displaced along a discordia line with a lower intercept at ~3.0 Ga. After filtering, there are three zircon analyses with ages ~3.0 Ga (**Fig. S-8d**). These do not form a single age population and we do not define a precise age from these zircon analyses, but note that two analyses have ^{207}Pb/^{206}Pb ages of ~2.96 Ga (2959 ± 11 Ma and 2963 ± 10 Ma), and one has an older age of ~3.00 Ga (2996 ± 15 Ma). These are similar to the distinct groups in ~3.0 Ga analyses in sample 208102, and we also interpret these as metamorphic zircons.

3.3 Orthogneiss sample 208144

The oldest age population in sample 208144 yields a weighted mean ^{207}Pb/^{206}Pb age of 3842 ± 7 Ma (n = 10; MSWD = 1.0; p = 0.41), which we interpret as the igneous age (**Fig. S-8e**). Like sample 208141, ^{207}Pb/^{206}Pb ages younger than this are discordant, reflecting both modern and ancient (~3.0 Ga) Pb loss. All seven analyses from the ~3.0 Ga group yield a weighted mean ^{207}Pb/^{206}Pb age of 2962 ± 7 Ma (MSWD = 1.8; p = 0.09; **Fig. S-8f**), which we interpret as the age of metamorphic zircon growth.

3.4 Leucogranite sample 208158

All screened analyses except one grain from sample 208158 (**Fig. S-9a**) are consistent with a single age population with a weighted mean ^{207}Pb/^{206}Pb age of 2966 ± 6 Ma (n = 17; MSWD = 0.85; p = 0.63). We interpret this as the igneous age of the leucogranite.

3.5 Leucogranite sample 208159

Like sample 208158, all screened analyses except one grain from sample 208159 (**Fig. S-9b**) comprise a single age population, which yielded a weighted mean ^{207}Pb/^{206}Pb age of 2976 ± 6 Ma (n = 22; MSWD = 1.3; p = 0.17). We interpret this as the igneous age of the leucogranite.

3.6 Leucogranite sample 208234

The oldest age population in sample 208234 yields a weighted mean ^{207}Pb/^{206}Pb age of 2976 ± 8 Ma (n = 11; MSWD = 1.9; p = 0.04), which we interpret as the igneous age of the leucogranite. Nine analyses between ~2.95 and 2.9 Ga do not form part of this population, and we interpret these grains to represent ~2.97 Ga zircons that were affected by later Pb loss. There is a further group of three analyses at ~2.7 Ga, which yield an upper concordia intercept age of 2693 ± 10 (MSWD = 0.22; p = 0.80). These are interpreted to reflect a second metamorphic event at ~2.7 Ga.

3.7 Summary of ^{207}Pb/^{206}Pb ages

Three main events are recorded in the zircon U-Pb ages discussed above. The first of these is the formation of the regional orthogneisses at ≥3.8 Ga, recorded by a ~3.8 Ga igneous age in sample 208102, and 3849 ± 6 Ma and 3841 ± 7 Ma igneous ages in 208141 and 208142, respectively. Similar ages have previously been reported for other orthogneisses near Ujaragssuit (Nutman *et al.*, 1993, 1996).

      Next, a metamorphic event at ~3.0 Ga caused formation of metamorphic zircons in the orthogneisses and generation of the leucogranites, likely via intracrustal melting. This event has previously been described as a ~2.96 Ga orogeny affecting the southern Isukasia portion of the Itsaq Gneiss Complex (Friend and Nutman, 2019) and has previously been recorded in metamorphic zircon overgrowths (Friend and Nutman, 2005; Nutman *et al.*, 2013) and both igneous zircons from the leucogranites and hydrothermal zircons within the Ujaragssuit chromitites themselves (Sawada *et al.*, 2023). Our data potentially suggests that the ~3.0 Ga event may have been more protracted than previously recognised, with the presence of some ~3.00–2.99 Ga metamorphic zircons in the orthogneisses, particularly sample 208102. However, the majority of ~3.0 Ga igneous leucogranite ages and metamorphic zircon growth events are younger, and indicate the bulk of metamorphic zircon in the orthogneisses formed contemporaneously with the intrusion of the leucogranites at ~2.97–2.96 Ga. A weighted mean of the igneous ages of leucogranites 208158, 208159, and 208234 along with ~2.97 Ga metamorphic zircon in samples 208102 and 208144, yields an age of 2970 ± 8 Ma (n = 5, using

weighted means from each sample; MSWD = 3.1; p = 0.02). We consider this the best estimate of the timing of ~3.0 Ga metamorphism at Ujaragssuit.
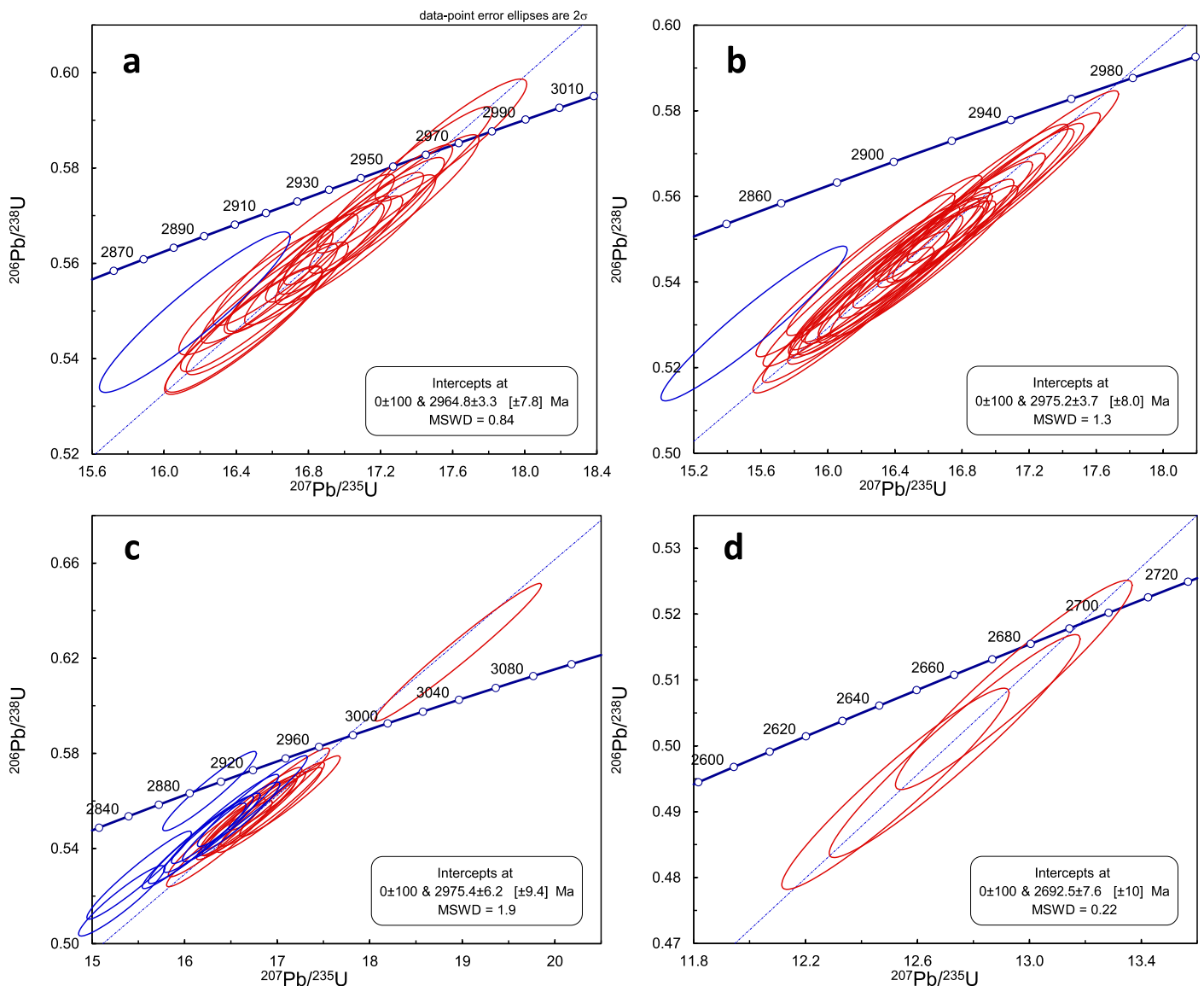

Figure S-9   Wetherill concordia plots for zircon U-Pb analyses from leucogranite samples. Intercept age calculations and symbols as in **Figure S-8**. **(a)** All analyses from sample 208158. **(b)** All analyses from sample 208158. **(c)** ~3.0 Ga analyses from sample 208234. **(d)** ~2.7 Ga analyses from sample 208234.

Finally, a second metamorphic event is recorded at ~2.7 Ga. The most reliable age for this event is given by the 2693 ± 12 Ma upper concordia intercept age of metamorphic zircon growth in leucogranite sample 208234. This metamorphic age has previously been recorded both in the Itsaq Gneiss Complex and its adjacent terranes and is commonly interpreted to reflect the juxtaposition of various terranes in the North Atlantic Craton of Greenland (Friend and Nutman, 2005, 2019; Kirkland *et al.*, 2018). However, we note that the timing of metamorphism from ~3.00 to ~2.97 Ga in the Itsaq Gneiss Complex that we record here closely mirrors the timing of a major metamorphic event in the Akia Terrane to the north (Friend and Nutman, 1994; Garde *et al.*, 2000; Gardiner *et al.*, 2019; Yakymchuk *et al.*, 2020), suggesting they may have shared metamorphic histories before 2.7 Ga.

4. Are ε^{184}Os Anomalies Real?

The mean ε^{184}Os for Ujaragssuit chromitite samples is distinct from zero within 2 standard errors (**Fig. 4**). However, the mean ε^{184}Os is also less than the uncertainty on an individual ε^{184}Os analysis and the ^{184}Os measurements are subject to large isobaric interference corrections from PtO$_2$ (Waterton *et al.*, 2023), which makes it difficult to confidently interpret as an anomaly. To investigate this further, we plotted the ε^{184}Os values as a function of both the total Os signal analysed and the proportion of the mass 232 signal (^{184}Os^{16}O$_3$) that originated from the major PtO$_2$ interference (^{198}Pt^{18}O^{16}O; **Fig. S-10**). There is no correlation with the total Os signal analysed, but we note that particularly low ε^{184}Os values are only associated with samples with low total Os on the filament. However, ε^{184}Os is weakly negatively correlated with the contribution of ^{198}Pt^{18}O^{16}O to the mass 232 signal, which suggests that an overcorrection of this interference might be the cause of the negative ε^{184}Os. The intercept of a regression of the data lies at ε^{184}Os = 0.51, suggesting that at zero ^{198}Pt^{18}O^{16}O interference the 'true' ε^{184}Os would be zero within analytical uncertainty.
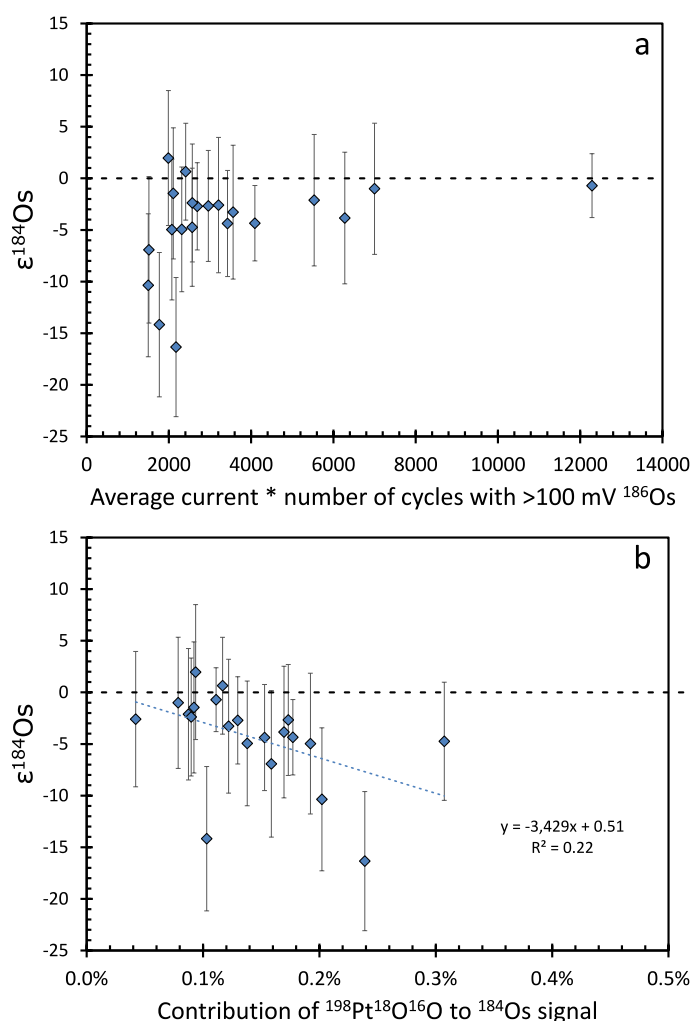
Figure S-10   Plots of ε^{184}Os against: **(a)** total Os signal, measured as the average voltage on ^{192}Os multiplied by the number of cycles successfully analysed for ^{186}Os; and **(b)** the proportion of the signal on mass 232 (^{184}Os^{16}O$_3$) that originated from the largest PtO$_2$ interference (^{198}Pt^{18}O^{16}O).

Supplementary Tables

Table S-2   Re-Os and HSE abundance data.

Table S-3   High precision Os data.

Table S-4   U-Pb data.

Tables S-2 to S-4 are available for download (.xlsx) from the online version of this article at http://doi.org/10.7185/geochemlet.2424.

Supplementary Information References

Appel, C.C., Appel, P.W.U., Rollinson, H.R. (2002) Complex chromite textures reveal the history of an early Archaean layered ultramafic body in West Greenland. *Mineralogical Magazine* 66, 1029–1041. https://doi.org/10.1180/0026461026660075

Ashton, K.E., Heaman, L.M., Lewry, J.F., Hartlaub, R.P., Shi, R. (1999) Age and origin of the Jan Lake Complex: a glimpse at the buried Archean craton of the Trans-Hudson Orogen. *Canadian Journal of Earth Sciences* 36, 185–208. https://doi.org/10.1139/e98-038

Barnes, S.J., Fiorentini, M.L. (2008) Iridium, ruthenium and rhodium in komatiites: Evidence for iridium alloy saturation. *Chemical Geology* 257, 44–58. https://doi.org/10.1016/j.chemgeo.2008.08.015

Bennett, V.C., Nutman, A.P., Esat, T.M. (2002) Constraints on mantle evolution from $^{187}Os/^{188}Os$ isotopic compositions of Archean ultramafic rocks from southern West Greenland (3.8 Ga) and Western Australia (3.46 Ga). *Geochimica et Cosmochimica Acta* 66, 2615–2630. https://doi.org/10.1016/S0016-7037(02)00862-1

Birck, J.L., Roy Barman, M.R., Capmas, F. (1997) Re-Os Isotopic Measurements at the Femtomole Level in Natural Samples. *Geostandards Newsletter* 20, 19–27. https://doi.org/10.1111/j.1751-908X.1997.tb00528.x

Brandon, A.D., Humayun, M., Puchtel, I.S., Leya, I., Zolensky, M. (2005) Osmium Isotope Evidence for an *s*-Process Carrier in Primitive Chondrites. *Science* 309, 1233–1236. https://doi.org/10.1126/science.1115053

Brandon, A.D., Walker, R.J., Puchtel, I.S. (2006) Platinum-osmium isotope evolution of the Earth's mantle: Constraints from chondrites and Os-rich alloys. *Geochimica et Cosmochimica Acta* 70, 2093–2103. https://doi.org/10.1016/j.gca.2006.01.005

Chatterjee, R., Lassiter, J.C. (2015) High precision Os isotopic measurement using N-TIMS: Quantification of various sources of error in $^{186}Os/^{188}Os$ measurements. *Chemical Geology* 396, 112–123. https://doi.org/10.1016/j.chemgeo.2014.12.014

Coggon, J.A., Luguet, A., Nowell, G.M., Appel, P.W.U. (2013) Hadean mantle melting recorded by southwest Greenland chromitite ^{186}Os signatures. *Nature Geoscience* 6, 871–874. https://doi.org/10.1038/ngeo1911

Coggon, J.A., Luguet, A., Fonseca, R.O.C., Lorand, J.P., Heuser, A., Appel, P.W.U. (2015) Understanding Re-Os systematics and model ages in metamorphosed Archean ultramafic rocks: A single mineral to whole-rock investigation. *Geochimica et Cosmochimica Acta* 167, 205–240. https://doi.org/10.1016/j.gca.2015.07.025

Cohen, A.S., Waters, F.G. (1996) Separation of osmium from geological materials by solvent extraction for analysis by thermal ionisation mass spectrometry. *Analytica Chimica Acta* 332, 269–275. https://doi.org/10.1016/0003-2670(96)00226-7

Creaser, R.A., Papanastassiou, D.A., Wasserburg, G.J. (1991) Negative thermal ion mass spectrometry of osmium, rhenium and iridium. *Geochimica et Cosmochimica Acta* 55, 397–401. https://doi.org/10.1016/0016-7037(91)90427-7

Day, J.M.D., Walker, R.J., Warren, J.M. (2017) ^{186}Os–^{187}Os and highly siderophile element abundance systematics of the mantle revealed by abyssal peridotites and Os-rich alloys. *Geochimica et Cosmochimica Acta* 200, 232–254. https://doi.org/10.1016/j.gca.2016.12.013

Friend, C.R.L., Nutman, A.P. (1994) Two Archaean granulite-facies metamorphic events in the Nuuk-Maniitsoq region, southern West Greenland: correlation with the Saglek block, Labrador. *Journal of the Geological Society* 151, 421–424. https://doi.org/10.1144/gsjgs.151.3.0421

Friend, C.R.L., Nutman, A.P. (2005) New pieces to the Archaean terrane jigsaw puzzle in the Nuuk region, southern West Greenland: Steps in transforming a simple insight into a complex regional tectonothermal model. *Journal of the Geological Society* 162, 147–162. https://doi.org/10.1144/0016-764903-161

Friend, C.R.L., Nutman, A.P. (2019) Tectono-stratigraphic terranes in Archaean gneiss complexes as evidence for plate

tectonics: The Nuuk region, southern West Greenland. *Gondwana Research* 72, 213–237. https://doi.org/10.1016/j.gr.2019.03.004

Garde, A.A., Friend, C.R.L., Nutman, A.R., Marker, M. (2000) Rapid maturation and stabilisation of middle Archaean continental crust: The Akia terrane, southern West Greenland. *Bulletin of the Geological Society of Denmark* 47, 1–27. https://doi.org/10.37570/bgsd-2000-47-01

Gardiner, N.J., Kirkland, C.L., Hollis, J., Szilas, K., Steenfelt, A., Yakymchuk, C., Heide-Jørgensen, H. (2019) Building Mesoarchaean crust upon Eoarchaean roots: the Akia Terrane, West Greenland. *Contributions to Mineralogy and Petrology* 174, 1–19. https://doi.org/10.1007/s00410-019-1554-x

Geo Labs (2001) *OKUM (Ontario Komatiite Ultramafic) Geo Lab's in-house reference material*.

Goderis, S., Brandon, A.D., Mayer, B., Humayun, M. (2017) Osmium isotopic homogeneity in the CK carbonaceous chondrites. *Geochimica et Cosmochimica Acta* 216, 8–27. https://doi.org/10.1016/j.gca.2017.05.011

Huber, P.J. (1981) *Robust statistics*. Wiley and Sons, New York. https://doi.org/10.1002/0471725250

JCGM (2008) JCGM 200:2008 International vocabulary of metrology — Basic and general concepts and associated terms (VIM) Vocabulaire international de métrologie — Concepts fondamentaux et généraux et termes associés (VIM). *International Organization for Standardization Geneva* 3, 104.

Kirkland, C.L., Yakymchuk, C., Hollis, J., Heide-Jørgensen, H., Danišík, M. (2018) Mesoarchean exhumation of the Akia terrane and a common Neoarchean tectonothermal history for West Greenland. *Precambrian Research* 314, 129–144. https://doi.org/10.1016/j.precamres.2018.06.004

Leys, C., Ley, C., Klein, O., Bernard, P., Licata, L. (2013) Detecting outliers: Do not use standard deviation around the mean, use absolute deviation around the median. *Journal of Experimental Social Psychology* 49, 764–766. https://doi.org/10.1016/j.jesp.2013.03.013

Liu, J., Pearson, D.G. (2014) Rapid, precise and accurate Os isotope ratio measurements of nanogram to sub-nanogram amounts using multiple Faraday collectors and amplifiers equipped with 10^{12} Ω resistors by N-TIMS. *Chemical Geology* 363, 301–311. https://doi.org/10.1016/j.chemgeo.2013.11.008

Ludwig, K.R. (2012) User's Manual for Isoplot, v3.75, A Geochronological Toolkit for Microsoft Excel. *Berkeley Geochronology Center Special Publications* 5, 1–75.

Luguet, A., Nowell, G.M., Pearson, D.G. (2008) $^{184}Os/^{188}Os$ and $^{186}Os/^{188}Os$ measurements by Negative Thermal Ionisation Mass Spectrometry (N-TIMS): Effects of interfering element and mass fractionation corrections on data accuracy and precision. *Chemical Geology* 248, 342–362. https://doi.org/10.1016/j.chemgeo.2007.10.013

Maier, W.D., Barnes, S.J., Campbell, I.H., Fiorentini, M.L., Peltonen, P., Barnes, S.-J., Smithies, R.H. (2009) Progressive mixing of meteoritic veneer into the early Earth's deep mantle. *Nature* 460, 620–623. https://doi.org/10.1038/nature08205

Meisel, T., Walker, R.J., Irving, A.J., Lorand, J.-P. (2001) Osmium isotopic composition of mantle xenoliths: A global perspective. *Geochimica et Cosmochimica Acta* 65, 1311–1323. https://doi.org/10.1016/S0016-7037(00)00566-4

Nier, A.O. (1950) A redetermination of the relative abundances of the isotopes of carbon, nitrogen, oxygen, argon, and potassium. *Physical Review* 77, 789–793. https://doi.org/10.1103/PhysRev.77.789

Nutman, A.P., Friend, C.R.L., Kinny, P.D., McGregor, V.R. (1993) Anatomy of an early Archean gneiss complex: 3900 to 3600 Ma crustal evolution in southern West Greenland. *Geology* 21, 415–418. https://doi.org/10.1130/0091-7613(1993)021<0415:AOAEAG>2.3.CO;2

Nutman, A.P., McGregor, V.R., Friend, C.R.L., Bennett, V.C., Kinny, P.D. (1996) The Itsaq Gneiss Complex of southern West Greenland; the world's most extensive record of early crustal evolution (3900-3600 Ma). *Precambrian Research* 78, 1–39. https://doi.org/10.1016/0301-9268(95)00066-6

Nutman, A.P., Bennett, V.C., Friend, C.R.L., Hidaka, H., Yi, K., Lee, S.R., Kamiichi, T. (2013) The Itsaq Gneiss Complex of greenland: Episodic 3900 to 3660 Ma juvenile crust formation and recycling in the 3660 to 3600 Ma Isukasian orogeny. *American Journal of Science* 313, 877–911. https://doi.org/10.2475/09.2013.03

Nutman, A.P., Bennett, V.C., Friend, C.R.L. (2015) Proposal for a continent "Itsaqia" amalgamated at 3.66 Ga and rifted apart from 3.53 Ga: Initiation of a Wilson cycle near the start of the rock record. *American Journal of Science* 315, 509–536. https://doi.org/10.2475/06.2015.01

Pearson, D.G., Woodland, S.J. (2000) Solvent extraction/anion exchange separation and determination of PGEs (Os, Ir, Pt, Pd, Ru) and Re-Os isotopes in geological samples by isotope dilution ICP-MS. *Chemical Geology* 165, 87–107. https://doi.org/10.1016/S0009-2541(99)00161-8

Reisberg, L., Dauphas, N., Luguet, A., Pearson, D.G., Gallino, R., Zimmermann, C. (2009) Nucleosynthetic osmium isotope anomalies in acid leachates of the Murchison meteorite. *Earth and Planetary Science Letters* 277, 334–344. https://doi.org/10.1016/j.epsl.2008.10.030

Rollinson, H., Appel, P.W.U., Frei, R. (2002) A Metamorphosed, Early Archaean Chromitite from West Greenland: Implications for the Genesis of Archaean Anorthositic Chromitites. *Journal of Petrology* 43, 2143–2170. https://doi.org/10.1093/petrology/43.11.2143

Sambridge, M., Lambert, D.D. (1997) Propagating errors in decay equations: Examples from the Re-Os system. *Geochimica et Cosmochimica Acta* 61, 3019–3024. https://doi.org/10.1016/S0016-7037(97)00130-0

Savard, D., Barnes, S.-J., Meisel, T. (2010) Comparison between nickel-sulfur fire assay Te co-precipitation and isotope dilution with high-pressure asher acid digestion for the determination of platinum-group elements, rhenium and gold. *Geostandards and Geoanalytical Research* 34, 281–291. https://doi.org/10.1111/j.1751-908X.2010.00090.x

Sawada, H., Morishita, T., Vezinet, A., Stern, R., Tani, K., Nishio, I., Takahashi, K., Pearson, D.G., Szilas, K. (2023) Zircon within chromitite requires revision of the tectonic history of the Eoarchean Itsaq Gneiss complex, Greenland. *Geoscience Frontiers* 14, 101648. https://doi.org/10.1016/j.gsf.2023.101648

Simonetti, A., Heaman, L.M., Hartlaub, R.P., Creaser, R.A., MacHattie, T.G., Böhm, C. (2005) U-Pb zircon dating by laser ablation-MC-ICP-MS using a new multiple ion counting Faraday collector array. *Journal of Analytical Atomic Spectrometry* 20, 677–686. https://doi.org/10.1039/b504465k

Söderlund, U., Johansson, L. (2002) A simple way to extract baddeleyite (ZrO_2). *Geochemistry, Geophysics, Geosystems* 3, 1–7. https://doi.org/10.1029/2001GC000212

Spencer, C.J., Kirkland, C.L., Taylor, R.J.M. (2016) Strategies towards statistically robust interpretations of in situ U-Pb zircon geochronology. *Geoscience Frontiers* 7, 581–589. https://doi.org/10.1016/j.gsf.2015.11.006

Stern, R.A., Bodorkos, S., Kamo, S.L., Hickman, A.H., Corfu, F. (2009) Measurement of SIMS instrumental mass fractionation of Pb isotopes during zircon dating. *Geostandards and Geoanalytical Research* 33, 145–168. https://doi.org/10.1111/j.1751-908X.2009.00023.x

Walker, R.J., Carlson, R.W., Shirey, S.B., Boyd, F.R. (1989) Os, Sr, Nd, and Pb isotope systematics of southern African peridotite xenoliths: Implications for the chemical evolution of subcontinental mantle. *Geochimica et Cosmochimica Acta* 53, 1583–1595. https://doi.org/10.1016/0016-7037(89)90240-8

Walker, R.J., Horan, M.F., Morgan, J.W., Becker, H., Grossman, J.N., Rubin, A.E. (2002) Comparative ^{187}Re-^{187}Os systematics of chondrites: Implications regarding early solar system processes. *Geochimica et Cosmochimica Acta* 66, 4187–4201. https://doi.org/10.1016/S0016-7037(02)01003-7

Waterton, P., Mungall, J., Pearson, D.G. (2021) The komatiite-mantle platinum-group element paradox. *Geochimica et Cosmochimica Acta* 313, 214–242. https://doi.org/10.1016/j.gca.2021.07.037

Waterton, P., Woodland, S., Pearson, D.G., Serre, S.H., Szilas, K. (2023) Probing the ^{186}Os/^{188}Os precision barrier: New recommended values for the DROsS reference material and an assessment of mixed 10^{11} and 10^{12} Ω amplifier arrays. *Geostandards and Geoanalytical Research* 1–24. https://doi.org/10.1111/ggr.12532

Wendt, I., Carl, C. (1991) The statistical distribution of the mean squared weighted deviation. *Chemical Geology* 86, 275–285. https://doi.org/10.1016/0168-9622(91)90010-T

Yakymchuk, C., Kirkland, C.L., Hollis, J.A., Kendrick, J., Gardiner, N.J., Szilas, K. (2020) Mesoarchean partial melting of mafic crust and tonalite production during high-T–low-P stagnant tectonism, Akia Terrane, West Greenland. *Precambrian Research* 339, 105615. https://doi.org/10.1016/j.precamres.2020.105615